Supplementary Information

Interfacial Electromechanics Predicts Phase Behavior of 2D Hybrid Halide Perovskites

Christopher C. Price[1], Jean-Christophe Blancon[2], Aditya D. Mohite[2], Vivek B. Shenoy[1,*]

[1]*Department of Materials Science and Engineering, University of Pennsylvania, Philadelphia 19104, USA*

[2]*Department of Chemical and Biomolecular Engineering, Rice University, Houston, Texas 77005, USA*

* Email: vshenoy@seas.upenn.edu

Supplementary Information

Table S1: A' cations used in quasi-2D perovskites; **studied in this work**.

Name (abbrev)	Formula	Structure
n-Propylammonium (PrA)	$C_3H_{10}N$	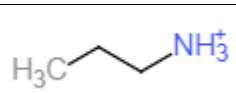
n-Butylammonium (BA)	$C_4H_{12}N$	
n-Pentylammonium (PA)	$C_5H_{14}N$	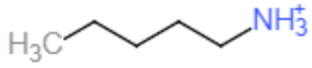
n-Hexlyammonium (HA)	$C_6H_{16}N$	
N,N-dimethylphenylene-p-diammonium (DPDA)	$C_8H_{14}N_2$	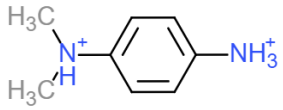
Phenyl-ethylammonium (PEA)	$C_8H_{12}N$	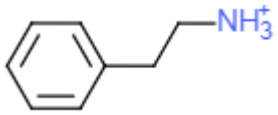
4-fluoro phenyl-ethylammonium (f-PEA)	$C_8H_{12}NF$	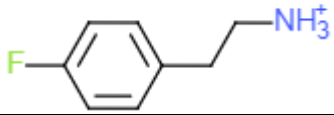
3-(aminomethyl)piperidinium (3-AMP)	$C_6H_{16}N_2$	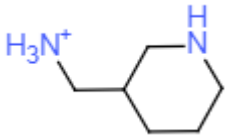
4-(aminomethyl)piperidinium (4-AMP)	$C_6H_{16}N_2$	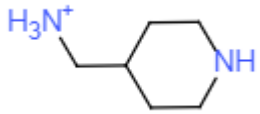

Table S2: Literature survey of maximum N-phases synthesized and characterized; $N_{crit.}$

Max N-phase synthesized and characterized	References
N = 1	[1], [2], [3]
N = 2	
N = 3	[4] [5] [6]
N = 4	[7], [8], [9], [10], [11], [12], [13], [14], [15]
N = 5	[16], [17], [18]
N = 6	
N = 7	[19], [20] *see introduction for discussion

Table S3: Electrostatic chemo-mechanical model parameters.

Symbol	Value	Units	Description
a_0	8.799	Å	In-plane lattice constants of tetragonal $MAPbI_3$[21]
c_0	8.799	Å	
b_0	12.688	Å	Out-of-plane lattice constant of tetragonal $MAPbI_3$ (corresponds to 2 N)
H_0^{pvsk}	-6.656	eV/formula unit	$Pb_{(s)} + \frac{3}{2}I_2 + \frac{1}{2}N_2 + C_{(s)} + 3H_2 \rightarrow CH_3NH_3PbI_3$
H_0^{BA}	-3.459	eV/formula unit	$4C_{(s)} + \frac{1}{2}N_2 + \frac{1}{2}I_2 + 6H_2 \rightarrow CH_3(CH_2)_3NH_3I$
$H_0^{PbI_2}$	-2.333	eV/formula unit	$Pb_{(s)} + I_2 \rightarrow PbI_2$
$H_0^{I_2}$	-2.720	eV/formula unit	
H_0^{Cs}	-1.874	eV/formula unit	
ε_r	12	ε_0	Average static dielectric constant for $MAPbI_3$ perovskites with surfaces[22]
C_{11}	280	Kbar	Calculated bulk elastic constants for $MAPbI_3$
C_{12}	70	Kbar	
C_{13}	160	Kbar	
C_{22}	330	Kbar	
γ_0	0.06	eV/Å^2	$\frac{1}{2A}(E_{bulk} - E_{slab} - \mu_{Cs} + \mu_I)$
f_{ss}	-0.043	eV/Å^2	$\frac{\partial \gamma_0}{\partial \varepsilon_{ip}}$
ρ_0	0.1		Gaussian disk spread
a_{dipole}	6.6	Å	BA : BA distance in the (010) plane.
Q_{dipole}	1.0	E	Interfacial dipole point charge
D_{dipole}	2.0	Å	Interfacial dipole sheet separation
$U_{interdigit}$	-0.138	eV/formula unit	$E_{periodic} - E_{slab}$
L_{BA}	5.85	Å	Width of BA layer (for determining atomic density)
V_0	n/a	Å^3	Unit cell volume $a_0 * c_0 * (Nb_0 + L_{BA})$

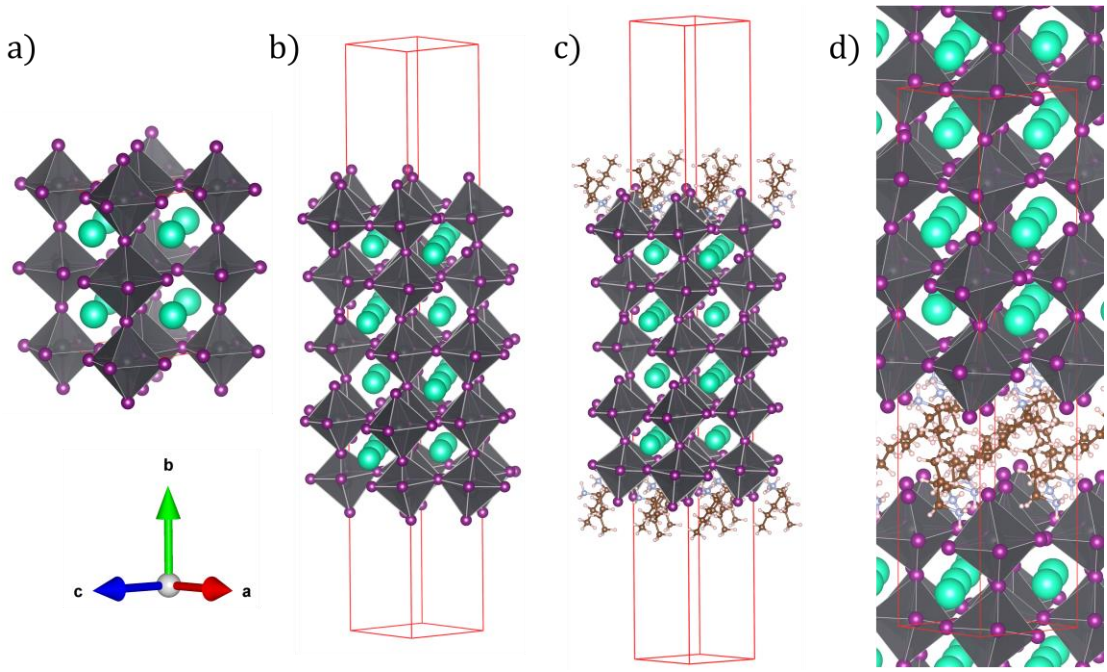

Figure S1. Sample atomistic structures used to extract model parameters. Pb atoms are gray, I atoms are purple, Cs atoms are green. **a)** Bulk perovskite with MA replaced for Cs. **b)** Symmetric 'bare' slab without any organics. **c)** BA-adsorbed perovskite symmetric slab. **d)** Fully periodic structure used for calculating $U_{interdigit}$.

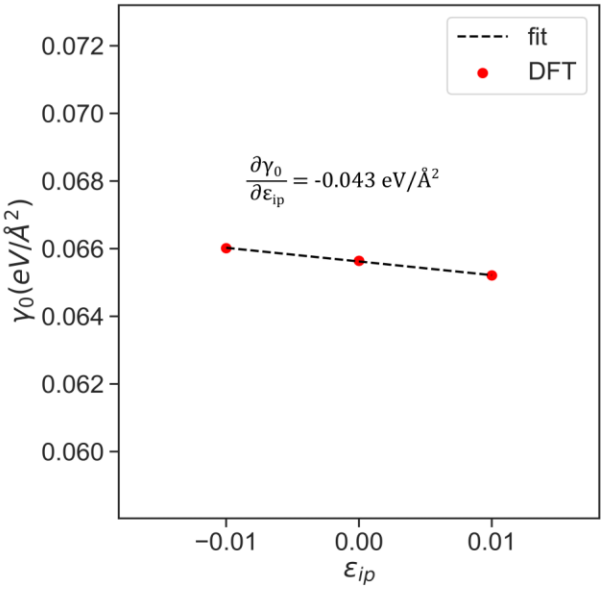

Figure S2. Calculation of the surface stress from the change in surface energy with in-plane strain.

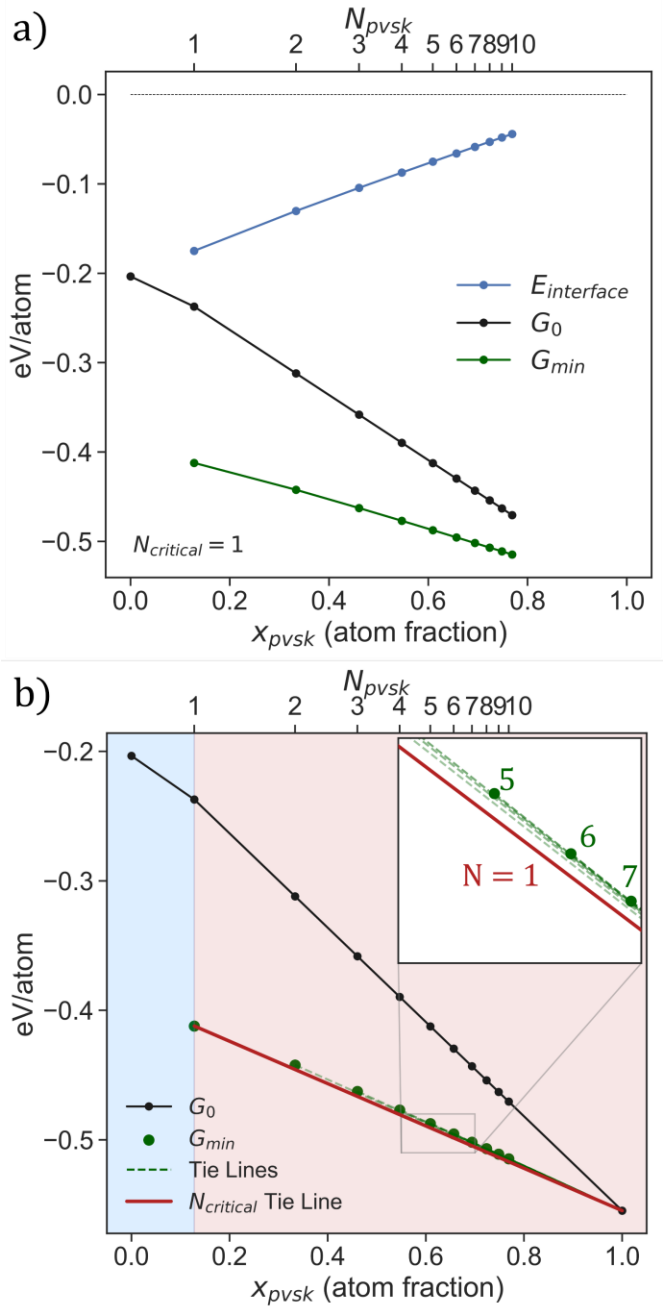

Figure S3. a) Component curves for G_{min} without U_E included in ΔH_{mix}. The independent bulk formation energy (black) and interfacial energy (blue) combine to give the energy of the ordered phases (green). **b)** Determination of N_{crit} without interfacial electrostatic interactions. The N = 1 + N = ∞ two-phase mixture is preferred across all compositions. This is determined by drawing tie lines between the bulk perovskite phase and all ordered phases, finding the two-phase mixture thermodynamically favored over other single-phase compounds.

Details of the Chemo-Mechanical Model

The perovskite slabs are assembled from the bulk tetragonal structures in Whitfield *et al.* by rotating the c-axis to the b-axis, following the convention in Kepenekian *et al.*[21,23] As discussed in Fig. 1 of the main text, the MA cations are replaced with Cs atoms to simulate rotational symmetry at 300 K and reduce computational cost. Sample unit cells of the bulk and slab geometries are shown in Fig. S1. All parameters and energies are calculated using density functional theory (DFT) calculations (Methods for details).

The surface energy γ_0 is calculated by subtracting the energy of the relaxed slab in Fig. S1b from the relaxed bulk energy in Fig. S1a, adjusted for the change in stoichiometry using the atomic reference energy of BCC Cs and molecular I_2 for the chemical potentials.

$$\gamma_0 = \frac{1}{2A}(E_{bulk} - E_{slab} - \mu_{Cs} + \mu_I)$$

where A is the area of the unit cell perpendicular to the surface. The adsorption energy γ_{ads} is calculated similarly using the unit cells in Fig. S1c and S1b:

$$\gamma_{ads} = \frac{1}{2A}(E_{slab} - E_{ads} - 4E_{BA})$$

The surface stress f_{ss} is calculated from the non-adsorbed perovskite slabs by taking the slope of a linear fit of the surface energy as function of in-plane strain ($\frac{\partial \gamma_0}{\partial \varepsilon_{ip}}$), relative to an equally strained bulk sample.[24] It was found that addition of the adsorbed molecules did not significantly change this relationship. All surface parameters were converged as a function of N and taken from symmetric slabs corresponding to N = 5 to minimize surface-surface interactions. The symmetric slab approach prevents net dipole moment interactions between periodic images across the vacuum space.

The elastic energy contribution is calculated *via* the following:

$$E_B = \frac{1}{2}(2C_{11}\varepsilon_{ip}^2 + C_{22}\varepsilon_{op}^2 + 4C_{12}\varepsilon_{op}\varepsilon_{ip} + 2C_{13}\varepsilon_{13}^2)$$

where C_{ij} are the bulk elastic coefficients calculated using the finite difference method and reported in Table S3. These values are in agreement with other reports.[25,26] To account for the

changing atom fraction of the elastic energy contribution with N, E_B is multiplied by x_{pvsk} (main text).

Finally, all quantities are converted to eV/atom using the N-dependent number of atoms per formula unit and the un-strained volume of the supercell V_0.

Electrostatic Energy of Opposing Interfacial Dipole Arrays

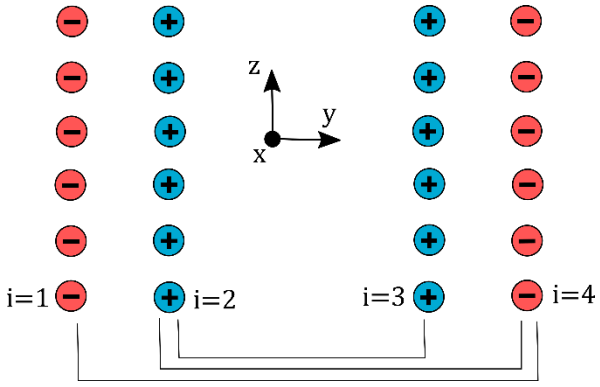

Figure S4. Schematic opposing lattices of point charges arranged to simulate interacting interfacial dipoles. The interactions counted in the model are shown using the black connectors; the $i = 2 : i = 4$ interaction is multiplied by 2 by symmetry.

Following previous works, we show the calculation of the electrostatic energy of two opposing dipole lattices.[27,28] The electrostatic energy between two parallel uniformly charged sheets which are infinitely periodic in their parallel dimensions is zero, while the energetic interactions between two individual dipoles at long distances falls off as $\sim\frac{1}{r^3}$, where r is the distance between the dipoles. For two infinite, parallel, and oppositely oriented point-charge dipole lattices, we expect that the electrostatic energy will fall between these limits. We start by solving the Poisson equation

$$\nabla^2\phi(x,y,z) = -\frac{\rho(x,y,z)}{\varepsilon_r} \quad (1)$$

where ϕ is the electric potential, ρ is the charge density, and ε_r is the static permittivity of the medium. Focusing on the N-dependent interaction, we break the dipole arrays into 4 parallel sheets of point charge square lattices with periodicity a_{dip}, 2 with positive charges and 2 with negative charges, such that the total system is charge neutral. We set the y dimension to be perpendicular to the sheet, consistent with the atomistic convention, so that the total charge density $\rho(x,y,z) =$

$\sum_{i=1}^{4}\sigma_i(x,z)\delta(y-y_i)$, where the index i enumerates each individual sheet at position y_i and $\sigma(x,z)$ is the in-plane charge density. Due to the principle of superposition, we can add the sum over sheets back in later and focus on a single sheet for now.

$\sigma(x,z)$ is composed of a charge motif which is periodic on the 2D lattice; to account for the periodicity, we will express the in-plane charge density as a Fourier series over the reciprocal lattice vectors $\vec{k}$ and solve the Poisson equation in Fourier space:

$$\sigma(x,z) = \sum_{k_{xz}} \tilde{\sigma}(k_x,k_z)\exp(ik_{xz}\cdot r_{xz}) \tag{2}$$

$$\tilde{\sigma}(k_x,k_z) = \frac{1}{A}\iint_{\frac{-a_{dip}}{2}}^{\frac{a_{dip}}{2}} dx\,dz\,\sigma(x,z)\exp(-ik_{xz}\cdot r_{xz}) \tag{3}$$

$$\tilde{\phi}\left(k_x,k_y,k_z\right) = \frac{\tilde{\rho}\left(k_x,k_y,k_z\right)}{\left(k_x^2+k_y^2+k_z^2\right)\varepsilon_0} = \frac{\tilde{\sigma}(k_x,k_z)\exp\left(-ik_y y_i\right)}{\left(k_x^2+k_y^2+k_z^2\right)\varepsilon_0} \tag{4}$$

Since we want to know the potential in terms of the inter-sheet distance, we transform k_y back to y using the Cauchy integral formula for a Lorentzian to get the mixed expression

$$\tilde{\phi}(k_x,y,k_z) = \frac{\tilde{\sigma}(k_x,k_z)\exp\left(-|y|\left|\vec{k}\right|\right)}{2\left|\vec{k}\right|\varepsilon_0} \tag{5}$$

This equation diverges at $k=0$, *i.e.* the long wavelength contribution which corresponds to the average charge density of the sheet σ_0. Since we know that the potential due to a uniform charge sheet is linear with distance and proportional to the average charge, we can separate the $k=0$ component when substituting for $\tilde{\sigma}(k_x,k_z)$. Adding back in the sum over 4 parallel sheets:

$$\begin{aligned}\phi(x,y,z) = \phi_0 &- \frac{1}{2\varepsilon_0}\sum_{i=1}^{4}\sigma_0|y-y_i| \\ &+ \sum_{k_{xz\neq 0}}\frac{\exp(ik_{xz}\cdot r_{xz})}{2\left|\vec{k}\right|\varepsilon_0}\sum_{i=1}^{4}\tilde{\sigma_i}(k_x,k_z)\exp(-|y-y_i||\vec{k}|)\end{aligned} \tag{6}$$

With an expression for the potential, we can then calculate the electrostatic potential energy per unit cell of the infinite sheets using the relation $U_E = \frac{1}{2}\int_V \rho\phi dV = \frac{1}{2}\iint_{\frac{-a}{2}}^{\frac{a}{2}} dx\,dz\int dy\,\rho\phi$. Writing out each term from (6) in this integral:

$$\frac{1}{2}\phi_0 \iint dA\, dy\, \sigma(x,z)\delta(y-y_i) = \frac{A}{2}\phi_0 \sum\nolimits_i \sigma_{0(i)}$$

$$\frac{-1}{4\varepsilon_0}\sum\nolimits_{i,j}\iint dA\, dy\ \sigma_i(x,z)\ \delta(y-y_i)\ \sigma_{0(j)}\ |y-y_j| = -\frac{A}{4\varepsilon_0}\sum\nolimits_{i,j}\sigma_{0(i)}\,\sigma_{0(j)}|y_i-y_j|$$

$$\frac{1}{2}\iint dA\, dy \sum\nolimits_i \sigma_i(x,z)\delta(y-y_i)\left[\sum\nolimits_{k_{xz}\neq 0}\frac{\exp(ik_{xz}\cdot r_{xz})}{2|\vec{k}|\varepsilon_0}\sum\nolimits_j \tilde{\sigma}_j(k_x,k_z)\exp\left(-|y-y_j||\vec{k}|\right)\right]$$

$$= \frac{1}{4\varepsilon_0}\iint dA\, dy \sum\nolimits_{k_{xz}\neq 0}\sum\nolimits_i \frac{\sigma_i(x,z)\exp(ik_{xz}\cdot r_{xz})}{|\vec{k}|}\sum\nolimits_j \sigma(k_x,k_z)\delta(y-y_i)\exp(-|y-y_j||\vec{k}|)$$

$$= \frac{1}{4\varepsilon_0}\iint dA\, dy \sum\nolimits_{k_{xz}\neq 0}\sum\nolimits_{i,j}\tilde{\sigma}_i(k_x,k_z)^*\tilde{\sigma}_j(k_x,k_z)\ \delta(y-y_i)\frac{\exp\left(-|y-y_j||\vec{k}|\right)}{|\vec{k}|}$$

$$= \frac{A}{4\varepsilon_0}\sum\nolimits_{k_{xz}\neq 0}\sum\nolimits_{i,j}\tilde{\sigma}_i(k_x,k_z)^*\tilde{\sigma}_j(k_x,k_z)\frac{\exp\left(-|y_i-y_j||\vec{k}|\right)}{|\vec{k}|}$$

Adding the final right hand side terms together gives the total electrostatic energy expression:

$$U_E = \frac{A}{2}\Big[\phi_0\sum\nolimits_i \sigma_{0(i)} - \frac{1}{2\varepsilon_0}\sum\nolimits_{i,j}\sigma_{0(i)}\,\sigma_{0(j)}\left|y_i-y_j\right| + \frac{1}{2\varepsilon_0}\sum\nolimits_{k_{xz}\neq 0}\sum\nolimits_{i,j}\tilde{\sigma}_i(k_x,k_z)^*\tilde{\sigma}_j(k_x,k_z)\frac{\exp\left(-\left|y_i-y_j\right||\vec{k}|\right)}{|\vec{k}|}\Big] \quad (7)$$

This expression rapidly simplifies for the desired case of opposing dipole sheets. The first term related to the potential integration is zero since the system is overall charge neutral (sum of the sheet averages = 0). The second term (linear term due to the average density) also drops out because the dipole sheets are oriented opposite and parallel to each other, with equal charge – this is the same result of zero potential for uniform and equally charged sheets. In the last term, we select only some of the summations over sheet indexes i and j. When $i = j$, the energetic contribution corresponds to the self-energy of assembling that charge sheet; in our model, this is captured by the surface energy. Since we are only interested in cross-surface interactions, we neglect terms with $i = j$. We also neglect terms with neighboring i, j, since the formation of the surface dipole is also accounted for by the surface energy. We neglect other periodic interactions in the y direction because these are accounted for in the interdigitation energy. Next, since the sum

is symmetric about interchange of i, j, we can extract a factor of 2 such that the total interacting sheet energy is:

$$U_E = \frac{A}{2\varepsilon_r}\sum_{k_{xz}\neq 0}\sum_{i<j}\frac{\tilde{\sigma}_i(k_x,k_z)^*\tilde{\sigma}_j(k_x,k_z)}{\left|\vec{k}\right|}\exp\left(-\left|y_i - y_j\right|\left|\vec{k}\right|\right) \quad (8)$$

In order to evaluate $\tilde{\sigma}$, we must choose a charge motif for the sheet. To avoid divergences associated with infinitesimal point charges and ensure the periodic component is separable from the perpendicular dimension, we choose a normalized 2D Gaussian disk $\sigma(x,z) = \frac{Q}{2\pi d^2}\exp\left(-\frac{x^2+z^2}{2\rho_0^2}\right)$ containing total charge Q and extent ρ_0, $\rho_0 \ll a_{dip}$. Then,

$$\tilde{\sigma}(k_x,k_z) = \frac{Q}{A}\exp(-\frac{(k_x^2+k_z^2)\rho_0^2}{2})$$

Finally, the energy U_E is converted from the fictitious dipole unit cell to eV/atom by dividing by the volume of the dipole unit cell $A|y_i - y_j|$ and then the atomic density of the atomic unit cell corresponding to one dipole unit cell. In practice, the expressions for $\tilde{\sigma}$ and U_E are evaluated numerically using the discrete fast fourier transform (FFT) functions available in SciPy and converged to appropriate grid resolutions.

REFERENCES

(1) Lin, Y.; Bai, Y.; Fang, Y.; Chen, Z.; Yang, S.; Zheng, X.; Tang, S.; Liu, Y.; Zhao, J.; Huang, J. Enhanced Thermal Stability in Perovskite Solar Cells by Assembling 2D/3D Stacking Structures. *J. Phys. Chem. Lett* **2018**, *9*, 654–658.

(2) Silver, S.; Yin, J.; Li, H.; Brédas, J.-L.; Kahn, A. Characterization of the Valence and Conduction Band Levels of *n* = 1 2D Perovskites: A Combined Experimental and Theoretical Investigation. *Adv. Energy Mater.* **2018**, *8*, 1703468.

(3) Mitzi, D. B. Synthesis, Crystal Structure, and Optical and Thermal Properties of

$(C_4H_9NH_3)_2MI_4$ (M = Ge, Sn, Pb). *Chem. Mater.* **1996**, *8*, 791–800.

(4) Raghavan, C. M.; Chen, T.-P.; Li, S.-S.; Chen, W.-L.; Lo, C.-Y.; Liao, Y.-M.; Haider, G.; Lin, C.-C.; Chen, C.-C.; Sankar, R.; Chang, Y.-M.; Chou, F.-C.; Chen, C.-W. Low-Threshold Lasing from 2D Homologous Organic–Inorganic Hybrid Ruddlesden–Popper Perovskite Single Crystals. *Nano Lett.* **2018**, *18*, 3221–3228.

(5) Tu, Q.; Spanopoulos, I.; Yasaei, P.; Stoumpos, C. C.; Kanatzidis, M. G.; Shekhawat, G. S.; Dravid, V. P. Stretching and Breaking of Ultrathin 2D Hybrid Organic–Inorganic Perovskites. *ACS Nano* **2018**, *12*, 10347–10354.

(6) He, X.; Wang, Y.; Li, K.; Wang, X.; Liu, P.; Yang, Y.; Liao, Q.; Zhai, T.; Yao, J.; Fu, H. Oriented Growth of Ultrathin Single Crystals of 2D Ruddlesden–Popper Hybrid Lead Iodide Perovskites for High-Performance Photodetectors. *ACS Appl. Mater. Interfaces* **2019**, *11*, 15905–15912.

(7) Cao, D. H.; Stoumpos, C. C.; Farha, O. K.; Hupp, J. T.; Kanatzidis, M. G. 2D Homologous Perovskites as Light-Absorbing Materials for Solar Cell Applications. *J. Am. Chem. Soc.* **2015**, *137*, 7843–7850.

(8) Leng, K.; Abdelwahab, I.; Verzhbitskiy, I.; Telychko, M.; Chu, L.; Fu, W.; Chi, X.; Guo, N.; Chen, Z.; Chen, Z.; Zhang, C.; Xu, Q.-H.; Lu, J.; Chhowalla, M.; Eda, G.; Loh, K. P. Molecularly Thin Two-Dimensional Hybrid Perovskites with Tunable Optoelectronic Properties Due to Reversible Surface Relaxation. *Nat. Mater.* **2018**, *17*, 908–914.

(9) Liu, J.; Leng, J.; Wu, K.; Zhang, J.; Jin, S. Observation of Internal Photoinduced Electron

and Hole Separation in Hybrid Two-Dimentional Perovskite Films. *J. Am. Chem. Soc.* **2017**, *139*, 1432–1435.

(10) Gélvez-Rueda, M. C.; Hutter, E. M.; Cao, D. H.; Renaud, N.; Stoumpos, C. C.; Hupp, J. T.; Savenije, T. J.; Kanatzidis, M. G.; Grozema, F. C. Interconversion between Free Charges and Bound Excitons in 2D Hybrid Lead Halide Perovskites. *J. Phys. Chem. C* **2017**, *121*, 26566–26574.

(11) Zhang, X.; Munir, R.; Xu, Z.; Liu, Y.; Tsai, H.; Nie, W.; Li, J.; Niu, T.; Smilgies, D.-M.; Kanatzidis, M. G.; Mohite, A. D.; Zhao, K.; Amassian, A.; Liu, S. Phase Transition Control for High Performance Ruddlesden–Popper Perovskite Solar Cells. *Adv. Mater.* **2018**, *10*, 1707166.

(12) Chen, A. Z.; Shiu, M.; Ma, J. H.; Alpert, M. R.; Zhang, D.; Foley, B. J.; Smilgies, D.-M.; Lee, S.-H.; Choi, J. J. Origin of Vertical Orientation in Two-Dimensional Metal Halide Perovskites and Its Effect on Photovoltaic Performance. *Nat. Commun.* **2018**, *9*, 1336.

(13) Tsai, H.; Nie, W.; Blancon, J.-C.; Stoumpos, C. C.; Asadpour, R.; Harutyunyan, B.; Neukirch, A. J.; Verduzco, R.; Crochet, J. J.; Tretiak, S.; Pedesseau, L.; Even, J.; Alam, M. A.; Gupta, G.; Lou, J.; Ajayan, P. M.; Bedzyk, M. J.; Kanatzidis, M. G.; Mohite, A. D. High-Efficiency Two-Dimensional Ruddlesden–Popper Perovskite Solar Cells. *Nature* **2016**, *536*, 312–316.

(14) Stoumpos, C. C.; Cao, D. H.; Clark, D. J.; Young, J.; Rondinelli, J. M.; Jang, J. I.; Hupp, J. T.; Kanatzidis, M. G. Ruddlesden–Popper Hybrid Lead Iodide Perovskite 2D Homologous Semiconductors. *Chem. Mater.* **2016**, *28*, 2852–2867.

(15) Chang, Y.-H.; Lin, J.-C.; Chen, Y.-C.; Kuo, T.-R.; Wang, D.-Y. Facile Synthesis of Two-Dimensional Ruddlesden–Popper Perovskite Quantum Dots with Fine-Tunable Optical Properties. *Nanoscale Res. Lett.* **2018**, *13*, 247.

(16) Stoumpos, C. C.; Soe, C. M. M.; Tsai, H.; Nie, W.; Blancon, J.-C.; Cao, D. H.; Liu, F.; Traoré, B.; Katan, C.; Even, J.; Mohite, A. D.; Kanatzidis, M. G. High Members of the 2D Ruddlesden-Popper Halide Perovskites: Synthesis, Optical Properties, and Solar Cells of $(CH_3(CH_2)_3NH_3)_2(CH_3NH_3)_4Pb_5I_{16}$. *Chem* **2017**, *2*, 427–440.

(17) Soe, C. M. M.; Nie, W.; Stoumpos, C. C.; Tsai, H.; Blancon, J.-C.; Liu, F.; Even, J.; Marks, T. J.; Mohite, A. D.; Kanatzidis, M. G. Understanding Film Formation Morphology and Orientation in High Member 2D Ruddlesden-Popper Perovskites for High-Efficiency Solar Cells. *Adv. Energy Mater.* **2018**, *8*, 1700979.

(18) Zhou, M.; Fei, C.; Sarmiento, J. S.; Wang, H. Manipulating the Phase Distributions and Carrier Transfers in Hybrid Quasi-Two-Dimensional Perovskite Films. *Sol. RRL* **2019**, *3*, 1800359.

(19) Soe, C. M. M.; Nagabhushana, G. P.; Shivaramaiah, R.; Tsai, H.; Nie, W.; Blancon, J.-C.; Melkonyan, F.; Cao, D. H.; Traoré, B.; Pedesseau, L.; Kepenekian, M.; Katan, C.; Even, J.; Marks, T. J.; Navrotsky, A.; Mohite, A. D.; Stoumpos, C. C.; Kanatzidis, M. G. Structural and Thermodynamic Limits of Layer Thickness in 2D Halide Perovskites. *Proc. Natl. Acad. Sci. U. S. A.* **2019**, *116*, 58–66.

(20) Mao, L.; Kennard, R. M.; Traore, B.; Ke, W.; Katan, C.; Even, J.; Chabinyc, M. L.; Stoumpos, C. C.; Kanatzidis, M. G. Seven-Layered 2D Hybrid Lead Iodide Perovskites. *Chem*

2019, *5*, 2593–2604.

(21) Whitfield, P. S.; Herron, N.; Guise, W. E.; Page, K.; Cheng, Y. Q.; Milas, I.; Crawford, M. K. Structures, Phase Transitions and Tricritical Behavior of the Hybrid Perovskite Methyl Ammonium Lead Iodide. *Sci. Rep.* **2016**, *6*, 35685.

(22) Sapori, D.; Kepenekian, M.; Pedesseau, L.; Katan, C.; Even, J. Quantum Confinement and Dielectric Profiles of Colloidal Nanoplatelets of Halide Inorganic and Hybrid Organic–Inorganic Perovskites. *Nanoscale* **2016**, *8*, 6369–6378.

(23) Kepenekian, M. L.; Traore, B.; Blancon, J.-C.; Pedesseau, L.; Tsai, H.; Nie, W.; Stoumpos, C. C.; Kanatzidis, M. G.; Even, J.; Mohite, A. D.; Tretiak, S.; Katan, C. Concept of Lattice Mismatch and Emergence of Surface States in Two-Dimensional Hybrid Perovskite Quantum Wells. *Nano Lett.* **2018**, *18*, 5603–5609.

(24) Müller, P.; Saùl, A.; Leroy, F. Simple Views on Surface Stress and Surface Energy Concepts. *Adv. Nat. Sci. Nanosci. Nanotechnol.* **2014**, *5*, 013002.

(25) de Jong, M.; Chen, W.; Angsten, T.; Jain, A.; Notestine, R.; Gamst, A.; Sluiter, M.; Krishna Ande, C.; van der Zwaag, S.; Plata, J. J.; Toher, C.; Curtarolo, S.; Ceder, G.; Persson, K. A.; Asta, M. Charting the Complete Elastic Properties of Inorganic Crystalline Compounds. *Sci. Data* **2015**, *2*, 150009.

(26) Faghihnasiri, M.; Izadifard, M.; Ghazi, M. E. DFT Study of Mechanical Properties and Stability of Cubic Methylammonium Lead Halide Perovskites ($CH_3NH_3PbX_3$, X = I, Br, Cl). *J. Phys. Chem. C* **2017**, *121*, 27059–27070.

(27) Bertaut, E. F. Electric Field and Energy in Dipole Lattices. *Phys. Rev.* **1953**, *91*, 415–415.

(28) Ismail-Beigi, S. 2D Periodic Charge Sheets: Electrostatics https://volga.eng.yale.edu/sites/default/files/files/2dsheets-electrostatics.pdf (accessed Jun 9, 2019).